

# $\delta$ -mapping algorithm coupled with WENO reconstruction for nonlinear elasticity in heterogeneous media

Zhenli Xu <sup>a</sup>, Peng Zhang <sup>b,\*</sup>, Ruxun Liu <sup>a</sup>

<sup>a</sup> *Department of Mathematics, University of Science and Technology of China, Hefei, Anhui 230026, PR China*

<sup>b</sup> *Shanghai Institute of Applied Mathematics and Mechanics, Shanghai University, Shanghai 200072, PR China*

Available online 2 March 2006

## Abstract

A newly proposed  $\delta$ -mapping algorithm is extended to solve compressional elastic wave propagation in nonlinear heterogeneous media, which is characterized by spatially varying flux functions. The algorithm is coupled with the weighted essentially non-oscillatory (WENO) reconstruction so that the property of high-accuracy is preserved. Without the  $\delta$ -mapping procedure, in contrast, the direct application of the WENO scheme is indicated to be deficient.

© 2006 IMACS. Published by Elsevier B.V. All rights reserved.

*Keywords:*  $\delta$ -mapping algorithm; WENO reconstruction; Nonlinear elastic waves; Layered media

## 1. Introduction

Recently, the  $\delta$ -mapping algorithm was proposed by Zhang and Liu [20,22] to deal with hyperbolic conservation laws with spatially varying flux functions. In the 1D scalar case, the mathematical theory of the algorithm was well developed and many favorable properties were proven. These include the consistency and monotonicity of numerical fluxes, and the obtaining of the entropy inequalities for strictly hyperbolic problems. Through the  $\delta$ -mapping procedure, the Runge–Kutta discontinuous Galerkin (RKDG) method was also extended and applied to the LWR traffic flow model with inhomogeneous road conditions [21]. These successful examples in the 1D scalar case indicate that the algorithm can be hopefully extended to systems.

For the extension, we write 1D hyperbolic conservation laws with spatially varying flux functions in the following general form:

$$U(x, t)_t + f(U(x, t), a(x))_x = 0, \quad (1)$$

where  $a(x)$  is a known scalar or vector function, usually representing some physical quantity or quantities. In traffic flow problems, for example,  $a(x)$  can be the number of lanes and the local maximum of the vehicle velocity [21]. For a uniform cell division  $\{I_j\}_{j=1}^N$  in spatial direction where  $I_j = [x_{j-1/2}, x_{j+1/2}]$ , the semi-discretization conservative

\* Corresponding author.

*E-mail address:* [pengzhang@ustc.edu](mailto:pengzhang@ustc.edu) (P. Zhang).

scheme of (1) can be written in the following form:

$$\frac{dU_j}{dt} + \frac{1}{\Delta x}(\hat{f}_{j+1/2} - \hat{f}_{j-1/2}) = 0, \quad (2)$$

in which the numerical fluxes  $\hat{f}_{j\pm 1/2}$  approximate the flux function  $f(U(x, t), a(x))$  at the cell boundaries  $x_{j\pm 1/2}$ . We suppose that  $\hat{f}_{j+1/2}$  is a function of  $\{U_i\}$  and  $\{a_i\}$  in the chosen stencil  $S_j = (x_{j-r}, \dots, x_{j+s})$ ,

$$\hat{f}_{j+1/2} = \hat{f}(U_{j-r}, \dots, U_{j+s}; a_{j-r}, \dots, a_{j+s}). \quad (3)$$

The basic idea of the  $\delta$ -mapping algorithm is to “standardize” the numerical flux function of (3), namely, it approximates a flux function in which the argument  $a$  is “frozen” or treated as a constant somewhere around  $x_{j+1/2}$ , thus  $\hat{f}$  can be given by a classical numerical flux function that is designed to approximate a “standard” flux function. For the purpose, we define a mapping in the following. That is, for each  $j$  we find a certain  $\tilde{a}_{j+1/2}$ , which represents an intermediate state between  $a_j$  and  $a_{j+1}$ ; then we define the operator

$$\delta_{j+1/2}: U_i \rightarrow \delta_{j+1/2}U_i, \quad \text{for } i = j - r, \dots, j + s,$$

such that

$$f(U_i, a_i) = f(\delta_{j+1/2}U_i, \tilde{a}_{j+1/2}), \quad \lambda_l(U_i, a_i)\lambda_l(\delta_{j+1/2}U_i, \tilde{a}_{j+1/2}) \geq 0. \quad (4)$$

Here  $\lambda_l(U, a)$  represents all eigenvalues of the Jacobian  $f_U(U, a)$ . It is natural to choose  $\tilde{a}_{j+1/2} = a(x_{j+1/2})$ ; or  $\tilde{a}_{j+1/2} = 0.5(a_j + a_{j+1})$ , if  $a(x)$  is discontinuous at  $x_{j+1/2}$ . The biased choices of  $\tilde{a}_{j+1/2} = a_j$  and  $\tilde{a}_{j+1/2} = a_{j+1}$  are also tested in the present paper.

In the case of the compressional elastic waves, we note that  $\delta_{j+1/2}U_i$  can be uniquely solved through the equality of (4), and that the required inequality is self-evident (see Section 3.1). In other problems (e.g., the traffic flow problem), however, these might not be ensured and more complexities would be considered [20,22,21].

Through the  $\delta$ -mapping algorithm that is defined by (4), these values  $U_i$  of  $a_i$  states are “uniformized” to be the values  $\delta_{j+1/2}U_i$  of a certain  $\tilde{a}_{j+1/2}$  state. Therefore, we define the function of (3) by a classical numerical flux function  $\tilde{f}$ , i.e.,

$$\hat{f}_{j+1/2} = \tilde{f}(\delta_{j+1/2}U_{j-r}, \dots, \delta_{j+1/2}U_{j+s}; \tilde{a}_{j+1/2}), \quad (5)$$

where  $\tilde{f}$  approximates the flux function  $f(\delta_{j+1/2}U, \tilde{a}_{j+1/2})$ . We note that  $\tilde{a}_{j+1/2}$  is fixed locally in the stencil  $S_j$ , thus  $\tilde{f}$  could be obtained through many well developed numerical techniques such as the discontinuous Galerkin method [3], the ENO and WENO reconstructions [7,14], which are all designed for the numerical approximation to standard conservation laws.

We stress two favorable properties of the  $\delta$ -mapping algorithm. For some appropriate choice of  $\tilde{a}_{j+1/2}$  and the replacement of  $\tilde{f}$  by the Godunov flux ( $r = 0$  and  $s = 1$ ) in the scalar case, we do acquire the exact Riemann solver from (5). Furthermore, it can be easily verified by (3)–(5) that  $\hat{f}$  is consistent with steady solutions such that, for  $i = j - r, \dots, j + s$ ,

$$\hat{f}(U_{j-r}, \dots, U_{j+s}; a_{j-r}, \dots, a_{j+s}) = f(U, \tilde{a}_{j+1/2}), \quad \text{if } f(U_i, a_i) \equiv f(U, \tilde{a}_{j+1/2}), \quad (6)$$

because  $\tilde{f}$  is supposed to be consistent with  $f(U, \tilde{a}_{j+1/2})$  such that

$$\tilde{f}(\delta_{j+1/2}U_{j-r}, \dots, \delta_{j+1/2}U_{j+s}; \tilde{a}_{j+1/2}) = f(U, \tilde{a}_{j+1/2}), \quad \text{if } \delta_{j+1/2}U_i \equiv U. \quad (7)$$

See also [20,22,21] for more details.

In the present paper, the  $\delta$ -mapping algorithm is coupled with the WENO reconstruction. This hybrid scheme is applied to solve compressional elastic waves in nonlinear heterogeneous media in the context of references [11,12,1,4]. In Section 2, the model equations of 1D problem are introduced. In Section 3, the procedures for the numerical implementation are detailed. In Section 4, considerable numerical examples are presented, which include those that demonstrate the capability of resolving simple waves in the Riemann problem (Section 4.1), those that simulate linear and nonlinear elastic waves in 1D heterogeneous media (Section 4.2), and those for accuracy test (Section 4.3). The extension to the 2D elasticity in heterogeneous media (which contains arbitrary-shaped interfaces) is also discussed briefly through one heuristic example (Section 4.4); more issues with this can be found in literatures (e.g., [15] and the references therein). In Section 5, we conclude the paper with several remarks.

## 2. Governing equations of 1D elasticity in heterogeneous media

We consider the system of the following two equations in 1D compressional elastic materials:

$$\varepsilon_t - u_x = 0, \tag{8}$$

$$(\rho u)_t - \sigma_x = 0, \tag{9}$$

where the unknown variables  $\varepsilon(x, t)$  and  $u(x, t)$  denote the strain and velocity, respectively; the density  $\rho(x)$  and the stress-strain relation  $\sigma = \sigma(\varepsilon, K(x))$  are known functions. It is well known that this system governs propagations of P-waves in the 1D elastic solid [10]. A elastic solid also supports shear waves (S-waves) in which the motion of the motion is orthogonal to the direction of wave propagation. In 1D situation, the equations of P-waves and S-waves are separated, and the equations of S-waves are essentially identical to (8)–(9).

When the problem is considered in a periodic medium that consists of alternating layers of two different materials, the functions  $\rho(x)$  and  $K(x)$  are regarded discontinuously as piecewise constants. Suppose that each layer is one unit thick, then they are given by

$$(\rho(x), K(x)) = \begin{cases} (\rho_A, K_A), & 2j \leq x < 2j + 1, \\ (\rho_B, K_B), & 2j + 1 \leq x < 2j + 2. \end{cases} \tag{10}$$

Besides, the stress  $\sigma$  is a continuous function of  $\varepsilon$  and  $K$ , as is given by

$$\sigma(\varepsilon, K) = K\varepsilon + \beta K^2 \varepsilon^2. \tag{11}$$

This same problem was discussed in [11,12]. Similar problems can be found in [1,4].

Corresponding to (1), we introduce the conservative variable  $Q = \rho u$ . Thus, the model equations of (8) and (9) can be written in the same conservation form of (1),

$$U_t + f(U, a)_x = 0, \tag{12}$$

with

$$U = (\varepsilon, Q), \quad f(U, a) = \begin{pmatrix} -Q/\rho \\ -\sigma(\varepsilon, K) \end{pmatrix}, \quad a = (\rho, K). \tag{13}$$

For fixed  $a$  we have the Jacobian matrix of  $f(U, a)$  and its two eigenvalues:

$$A(U, a) \equiv f_U(U, a) = \begin{pmatrix} 0 & -1/\rho \\ -\sigma_\varepsilon & 0 \end{pmatrix}, \quad \lambda_1(U, a) = -c, \quad \lambda_2(U, a) = c, \tag{14}$$

where  $c = \sqrt{\sigma_\varepsilon/\rho}$  is the sound speed, and  $\sigma_\varepsilon$  is the first order derivative of  $\sigma$  with respect to  $\varepsilon$ . Let  $R$  denote the eigen-matrix which consists of two linearly independent right eigenvectors:  $R(U, a) = (r_1(U, a), r_2(U, a))$ , then the Jacobian  $A$  is diagonalized as the follows:

$$R^{-1}(U, a)A(U, a)R(U, a) = \Lambda(U, a),$$

with

$$R(U, a) = \begin{pmatrix} \frac{1}{c\rho} & -\frac{1}{c\rho} \\ 1 & 1 \end{pmatrix}, \quad R^{-1}(U, a) = \begin{pmatrix} \frac{c\rho}{2} & \frac{1}{2} \\ -\frac{c\rho}{2} & \frac{1}{2} \end{pmatrix}, \quad \Lambda(U, a) = \begin{pmatrix} -c & 0 \\ 0 & c \end{pmatrix}. \tag{15}$$

This diagonalization will be applied for the characteristic decomposition in Section 3.

The initial and boundary conditions will be given in Section 4 for numerical implementation. To learn more about the physical background of this problem, see [11,12,1,4]. The wave propagation properties are detailed in [11].

## 3. Application of $\delta$ -mapping algorithm to elastic system

In accordance with the procedures of (2)–(5) (Section 1), we design the numerical scheme for conservation system (12). For this purpose we first map all relevant values  $U_i$  of (3) onto the  $\tilde{a}_j$  state by solving (4), so that we obtain  $\delta_j U_i$ . Then we compute  $\hat{f}_{j+1/2}$  of (5) by the fifth-order accurate WENO reconstruction. This will involve six point values of  $\delta_{j+1/2} U_i$  and precisely  $r = 2$  and  $s = 3$  in (3)–(5).

A complete numerical scheme of the model system is detailed in the following sections.

### 3.1. Mapping solution variables of $a_i$ states onto $\tilde{a}_{j+1/2}$ state

By (4) and (13), we have, for  $i = j - 2, \dots, j + 3$ ,

$$Q_i / \rho_i = \delta_{j+1/2} Q_i / \tilde{\rho}_{j+1/2}, \quad \sigma(\varepsilon_i, K_i) = \sigma(\delta_{j+1/2} \varepsilon_i, \tilde{K}_{j+1/2}), \quad (16)$$

where  $(\tilde{\rho}_{j+1/2}, \tilde{K}_{j+1/2}) = \tilde{a}_{j+1/2}$ . We solve  $\delta_{j+1/2} Q_i$  and  $\delta_{j+1/2} \varepsilon_i$  according to two different cases of (11), as is proceeded in the following.

For linear materials with  $\beta = 0$ , (16) is easily solved by

$$\delta_{j+1/2} Q_i = \tilde{\rho}_{j+1/2} Q_i / \rho_i, \quad \delta_{j+1/2} \varepsilon_i = \frac{\sigma(\varepsilon_i, K_i)}{\tilde{K}_{j+1/2}}. \quad (17)$$

For nonlinear materials with  $\beta > 0$ , since  $\delta_{j+1/2} \varepsilon_i > 0$ , (16) can be solved uniquely by

$$\delta_{j+1/2} Q_i = \tilde{\rho}_{j+1/2} Q_i / \rho_i, \quad \delta_{j+1/2} \varepsilon_i = \frac{(1 + 4\beta\sigma(\varepsilon_i, K_i))^{1/2} - 1}{2\beta\tilde{K}_{j+1/2}}. \quad (18)$$

We note that the inequality of (4) is self-evident in the solution.

### 3.2. Characteristic-wise WENO reconstruction through flux splitting

To derive the numerical flux  $\hat{f}_{j+1/2}$  from the function of (5), it seems that system (12) is standardized locally at  $x_{j+1/2}$ , to be the following:

$$U_t + f(U, \tilde{a}_{j+1/2})_x = 0. \quad (19)$$

Accordingly, we reconstruct the numerical flux function  $\hat{f}_{j+1/2}$  by the WENO method with  $U = \{\delta_{j+1/2} U_i\}$ , which are given by (17) or (18) for  $i = j - 2, \dots, j + 3$ . This reconstruction is proceeded as follows:

(1) Linearize the Jacobian of (19) at  $x_{j+1/2}$  by choosing the arithmetic mean  $U_{j+1/2} = 0.5(\delta_{j+1/2} U_j + \delta_{j+1/2} U_{j+1})$ , and proceed the characteristic decomposition of  $A(U_{j+1/2}, \tilde{a}_{j+1/2})$  following (14)–(15) so as to obtain

$$R = R(U_{j+1/2}, \tilde{a}_{j+1/2}), \quad R^{-1} = R^{-1}(U_{j+1/2}, \tilde{a}_{j+1/2}), \quad c = c(U_{j+1/2}, \tilde{a}_{j+1/2}).$$

(2) Multiply (19) with  $R^{-1}$  and make the transformation:  $V = R^{-1}U$ ,  $g = R^{-1}f(U, \tilde{a}_{j+1/2})$ ; and compute

$$V_i = R^{-1} \delta_{j+1/2} U_i, \quad g_i = R^{-1} f(\delta_{j+1/2} U_i, \tilde{a}_{j+1/2}), \quad \text{for } i = j - 2, \dots, j + 3.$$

We then proceed the following local Lax–Friedrichs flux splitting:

$$g_i^+ = \frac{1}{2}(g_i + \alpha_{j+1/2} V_i), \quad g_i^- = \frac{1}{2}(g_i - \alpha_{j+1/2} V_i), \quad \text{for } i = j - 2, \dots, j + 3.$$

Since  $|\lambda_1| = |\lambda_2| = c$ , in the above we choose a mutual viscosity coefficient for each component of the characteristic variables,

$$\alpha_{j+1/2} = \max(c(\delta_{j+1/2} U_j, \tilde{a}_{j+1/2}), c(\delta_{j+1/2} U_{j+1}, \tilde{a}_{j+1/2})).$$

(3) With  $v_i = g_i^+$ ,  $i = j - 2, \dots, j + 2$ , compute  $v_{j+1/2}^-$  component by component through the WENO reconstruction, and then set  $\hat{g}_{j+1/2}^+ = v_{j+1/2}^-$ . With  $v_i = g_i^-$ ,  $i = j - 1, \dots, j + 3$ , compute  $v_{j+1/2}^+$  similarly through the WENO reconstruction and then set  $\hat{g}_{j+1/2}^- = v_{j+1/2}^+$ . Thus we have

$$\hat{g}_{j+1/2} = \hat{g}_{j+1/2}^+ + \hat{g}_{j+1/2}^-.$$

(4) Form the flux by transforming back into physical space:

$$\hat{f}_{j+1/2} = R \hat{g}_{j+1/2}.$$

Finally, for the temporal discretization of (2), we apply the third-order accurate TVD Runge–Kutta method. We note that the WENO reconstruction along with the TVD Runge–Kutta discretization is not detailed in the above since

they can be found widely in many publications, e.g., in [18,9,8,2,17] for upwind WENO schemes, and in [13,16] for central WENO schemes. According to considerable numerical experience [6], it is suggested that the stability for the WENO scheme is ensured under the following CFL condition:

$$\frac{\Delta t^n}{\Delta x} \alpha^n \leq 0.6, \tag{20}$$

where  $\alpha^n$  is the maximum of  $\alpha_{j+1/2}$  taken over all  $j$  at  $t = t^n$ . Although the problem is with spatially varying flux functions, this stability condition is inherited by the proposed  $\delta$ -mapping algorithm in that the equality of (20) is always taken in numerical implementation.

#### 4. Numerical examples

In Section 4.1, two examples of the Riemann problem are designed for mathematical purpose, but they are unnecessarily the physical reality. With clear wave profiles, the examples show high resolution property and indicate the credibility of the proposed numerical scheme. Furthermore, convergence to (exact) smooth solution with high order accuracy is also indicated (Section 4.3). These are important for the scheme to be applied to solve application problems, for which the exact solution can generally not be obtained. In solving the 1D elasticity in heterogeneous media (Section 4.2), the numerical results are comparable with those given in [1,4,12]; the example for solving the 2D elasticity in heterogeneous media (Section 4.4) is also comparable with that in [10].

We note that the WENO scheme that is without the  $\delta$ -mapping procedure (or by defining  $\delta_{j+1/2}u \equiv u$  in our scheme) is shown to be inefficient (Sections 4.1 and 4.2). Finally, for the choice of the intermediate state  $\tilde{a}_{j+1/2}$  in our scheme, we adopt  $\tilde{a}_{j+1/2} = 0.5(a_j + a_{j+1})$  in all of our examples except for two figures respectively in Sections 4.2 and 4.3, where two biased choices of  $\tilde{a}_{j+1/2} = a_j$  and  $\tilde{a}_{j+1/2} = a_{j+1}$  are compared.

##### 4.1. Resolution of waves in Riemann problem

For the following two numerical examples, the Riemann problem is given by the data:

$$(\varepsilon(x, 0), Q(x, 0)) = \begin{cases} (0.3, -0.3), & x < 0, \\ (0.1, -0.1), & \text{otherwise.} \end{cases} \tag{21}$$

These are initial value problems and therefore no boundary conditions are needed. As indicated in [21] and the references therein, system (12) can be similarly rewritten as a standard  $3 \times 3$  system with an extra characteristic field  $\lambda = 0$ , thus three waves are expected in numerical results. The exact Riemann solution of linear system (12) was also obtained with three waves in [11].

**Example 1** (Linear case,  $\Delta x = 0.1$ , Fig. 1). For (12) with  $\beta = 0$  in (11), the vector function  $a(x)$  is taken as

$$(\rho(x), K(x)) = \begin{cases} (1, 1), & x < 0, \\ (3, 3), & \text{otherwise.} \end{cases} \tag{22}$$

In this problem, besides the contact discontinuity that coincides with the interface  $x = 0$ , one linear wave propagates backward with the speed  $\lambda_1 = -1$ , whereas the other propagates forward with the speed  $\lambda_2 = 1$ .

In Fig. 1(a), these three waves are highly resolved by the proposed numerical scheme. In contrast, the direct application of the WENO scheme (without the  $\delta$ -mapping) is incapable of resolving the contact discontinuity  $x = 0$ , as is shown in Fig. 1(c), where the non-physical “blow-up” in  $Q$  can be hardly suppressed even with sufficiently small  $\Delta t^n$ , say with  $\Delta t^n = 0.1 \Delta x / \alpha^n$ .

The different results of the two algorithms can be well explained through the comparison between Fig. 1(b) and (d). Since  $-u$  and  $-\sigma$  are the components of the flux vector  $f$ ,  $u$  and  $\sigma$  must be continuous at the interface after the wave breaking, even through they are discontinuous initially. This conclusion is made according to the Rankine–Hugoniot conditions which are applied for the conservation at the interface  $x = 0$ . In Fig. 1(b), we note that this feature is highly resolved because the numerical flux of the proposed scheme is consistent with steady flows, as is stated in (6) and (7). In contrast, the non-physical “blow-up” (or oscillations) near the interface in Fig. 1(d) can be hardly suppressed since the WENO scheme itself is consistent only with trivial solutions, but not with steady flows in general.

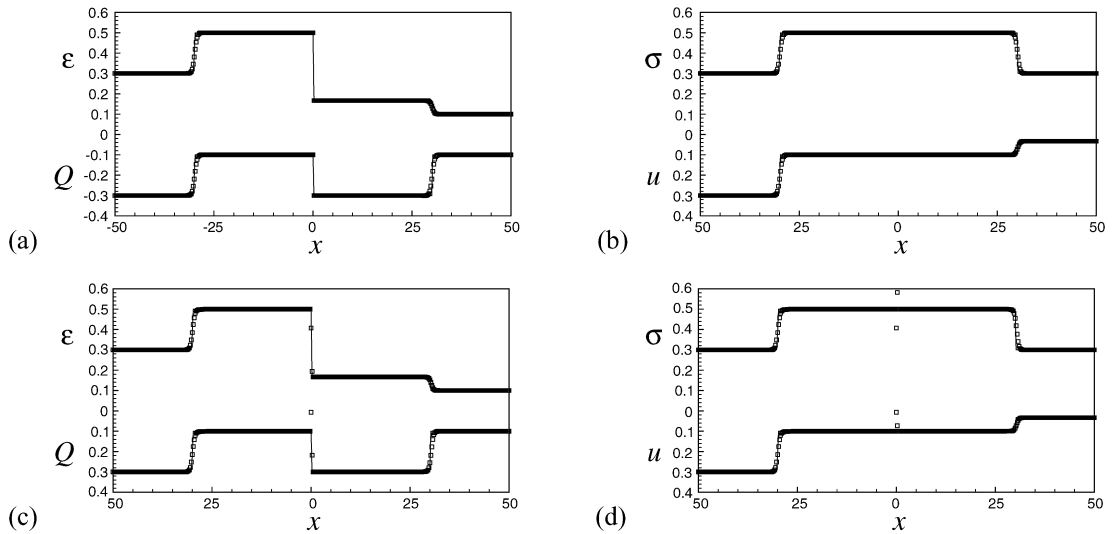


Fig. 1. Linear waves of Riemann solution at  $t = 30$ , 400 grid points, (a), (b) with  $\delta$ -mapping; (c), (d) without  $\delta$ -mapping.

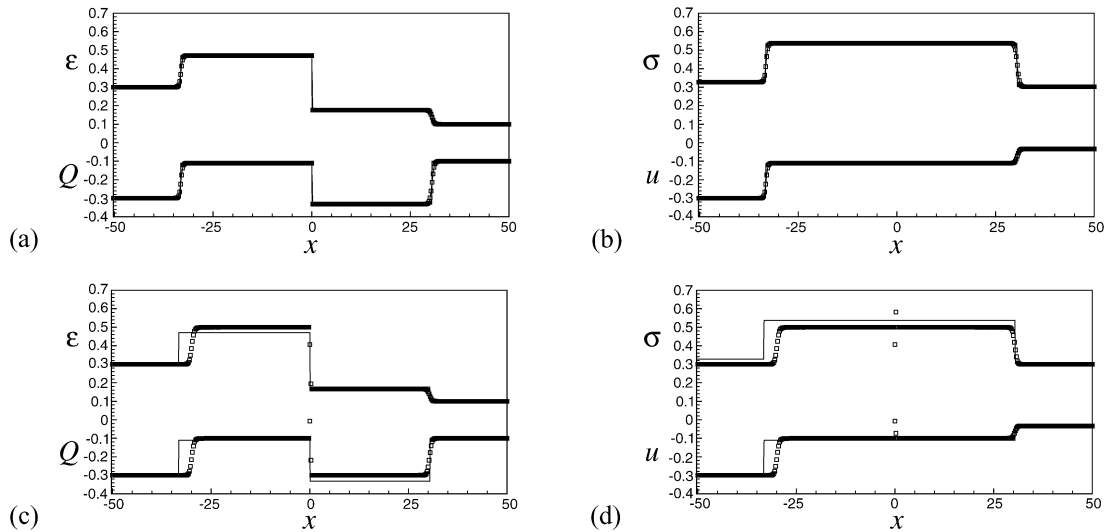


Fig. 2. Nonlinear waves of Riemann solution at  $t = 30$ , 400 grid points, (a), (b) with  $\delta$ -mapping; (c), (d) without  $\delta$ -mapping.

In the above, the comparison should be similar (probably with numerical results no better) if the WENO scheme is replaced by other classical numerical methods that are designed for solving standard hyperbolic conservation laws. Therefore, we conclude that the  $\delta$ -mapping algorithm is a crucial step whereby a classical scheme could be coupled in solving hyperbolic conservation laws with spatially varying flux functions. In the scalar case, we note that this argument is strongly supported by those numerical schemes that were developed in [20,22,21].

**Example 2** (Nonlinear case,  $\Delta x = 0.1$ , Fig. 2). For nonlinear system (12) with  $\beta = 0.3$  in (11), the vector function  $a(x)$  is given by

$$(\rho(x), K(x)) = \begin{cases} (1, 1), & x < 0, \\ (3, 3), & \text{otherwise.} \end{cases} \tag{23}$$

The numerical results are shown in Fig. 2. In this example, our comments on numerical results and the comparison between the two algorithms are similar to those in Example 1, except that two shocks (instead of two contact discontinuities) moving in opposite directions away from the interface are observed.

#### 4.2. Application examples

We consider a periodic medium that consists of alternating layers of two different materials, for which the parameters of (10) are given in each example. The initial data are taken as

$$\varepsilon(x, 0) = 0, \quad u(x, 0) = 0, \quad \text{or} \quad U(x, 0) = 0;$$

additionally, a boundary condition at  $x = 0$  is applied and given by

$$u(0, t) = \begin{cases} -0.2(1 + \cos(\pi(t - 30)/30)) & \text{if } t \leq 60, \\ 0 & 60 < t < 70. \end{cases} \quad (24)$$

This boundary condition is a description of stretching the material by pulling the left edge outward for  $0 < t < 60$ , resulting in elastic waves that propagate through the material rightwards. The velocity retrieves its initial value with  $u(0, t) = u(0, 0) = 0$  for  $t \geq 60$ , and as a consequence the left boundary restores to its initial state with  $U(0, t) = U(0, 0) = 0$  for  $t > t_0$ , where  $t_0$  should be slightly larger than 60. To describe this recovery at the left boundary, it is enough to set  $u(0, t) = 0$  for  $t > t_0$  with  $t_0 = 70$ , as is indicated in (24). Thereafter the right-going wave is supposed to propagate through an essentially infinite medium, and thus we apply the periodic boundary conditions (for  $t \geq 70$ ) to observe long time behavior of the propagation.

We state with emphasis on the numerical treatment of the boundary conditions during the perturbation and recovery period  $0 < t < 70$ . To reflect this physically unique process, the numerical flux at the left boundary should be fixed such that they are given exactly, i.e.,  $\hat{f}_{1/2} = (-u, -\sigma)^T|_{x=0}$ . Furthermore, the WENO reconstruction requires three cells on the left side of the concerned cell interface, thus two ghost point values in  $I_{-1}$  and  $I_0$  are needed to obtain  $\hat{f}_{3/2}$  and  $\hat{f}_{5/2}$ . Considering that  $u$  and  $\sigma$  in the flux function are smoother, we acquire them from the following second-order extrapolation:

$$u_k = 2u_{k+1} - u_{k+2}, \quad \sigma_k = 2\sigma_{k+1} - \sigma_{k+2}, \quad k = -1, 0.$$

Accordingly,  $\varepsilon_k$  and  $Q_k$  are obtained through (11) and the relation  $Q = \rho u$ .

In the following, we adopt exactly the same data of physical parameters as those in [11], so that one can validate the numerical results computed by the proposed scheme through comparison.

**Example 3** (*Heterogeneous linear material*,  $\Delta x = 0.125$ , Fig. 3). We set  $\beta = 0$  in (11), and other parameters in (10) are specified as follows:

$$\rho_A = 1, \quad \rho_B = 3; \quad K_A = 1, \quad K_B = 3.$$

The numerical results of the strain and stress at time  $t = 60$  and 90 are shown in Fig. 3. In the observation, Fig. 3(a)–(d) indicate that the waves are of right-going and the shapes of the strain and stress keep essentially unchanged. At each layer interface, the strain  $\varepsilon$  is discontinuous in contrast to the stress  $\sigma$  which is continuous and thus much smoother.

These features as well as the figure profiles are completely in accordance with data in [11]. In Fig. 3(e) and (f), on the other hand, we see significant non-physical oscillations that are due to the direct application of the WENO scheme without the  $\delta$ -mapping procedure.

**Example 4** (*Heterogeneous nonlinear material*,  $\Delta x = 0.05$ , Figs. 4–6). We set  $\beta = 0.3$ , and the data in (10) are given as

$$\rho_A = 1, \quad \rho_B = 3; \quad K_A = 1, \quad K_B = 3.$$

The strain and stress at  $t = 120$  and 240 are shown in Fig. 4. In Fig. 4(a)–(d), the numerical results are computed by the proposed scheme and accurately we see the hump in stress steepen and the figure profiles break up into a train of solitary waves. In the development up to  $t = 840$ , 1500 and 2850, for which the numerical results are shown in Fig. 5, it is very interesting to see these waves separate each other. Again, these results including the wave number and lengths are completely in accordance with those in [11]. In comparison, the direct application of the WENO scheme fails to distinguish these waves (Fig. 4(e) and (f)).

Finally, we show that the different choices of intermediate state  $\tilde{a}_{j+1/2}$  will make little difference in numerical results. For the same other parameters of this example and at  $t = 1500$ , the velocity  $u$  and the stress  $\sigma$  are used for the comparison as shown in Fig. 6, because they (as the components of  $-f$ ) are most sensitive to errors.

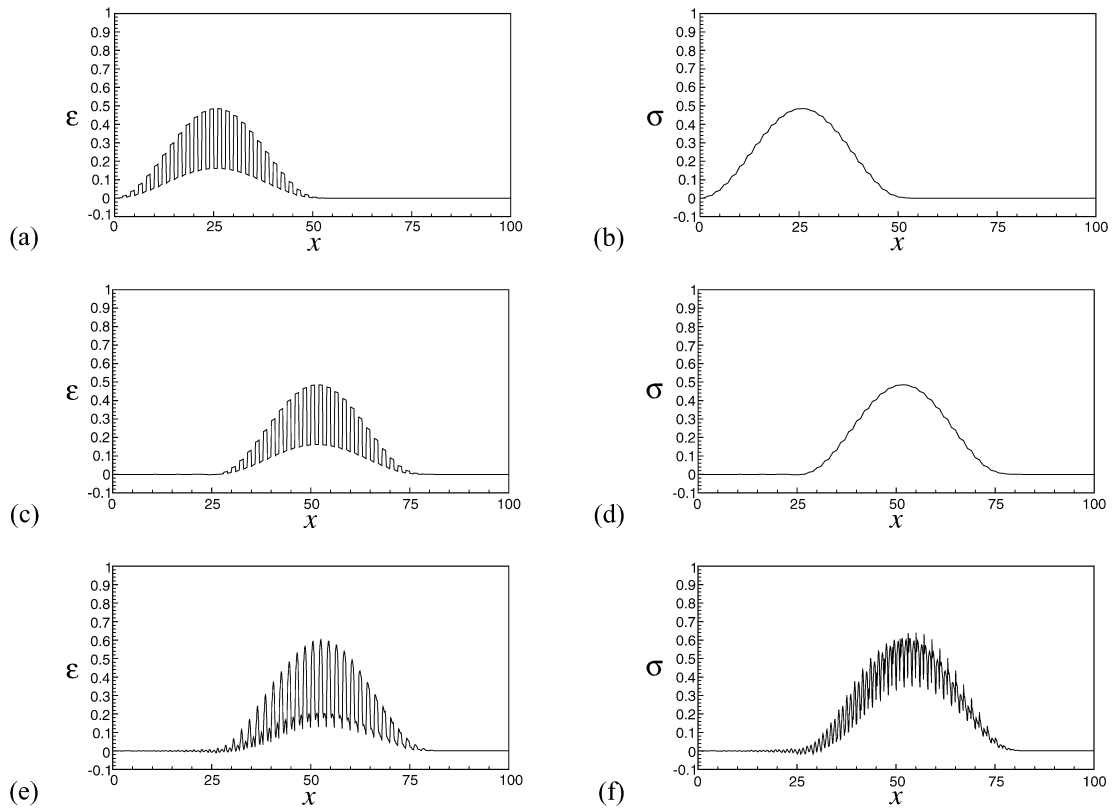


Fig. 3. The strain and stress, (a)–(d) at  $t = 60$  and  $t = 90$  with  $\delta$ -mapping; (e), (f) at  $t = 90$  without  $\delta$ -mapping.

4.3. Accuracy test

For this accuracy test, we specify the coefficients  $\rho(x)$  and reset the strain and stress relation, so as to obtain smooth solutions of (12). For the linear case, we choose  $\rho = (6x^2 + 2)(2 + x^2)^{-1}$ , and  $\sigma = (1 + x^2)\epsilon$ , so that

$$\epsilon(x, t) = -2xe^{-t}, \quad u(x, t) = (2 + x^2)e^{-t}. \tag{25}$$

For the nonlinear case, we choose  $\rho = (28 + 26x + 6x^2)(6 + 4x + x^2)^{-1}$ , and  $\sigma = (\frac{5}{4} + \frac{x}{2})\epsilon^2$ , then

$$\epsilon(x, t) = \frac{12x + 24}{(t + 1)^2}, \quad u(x, t) = -\frac{12x^2 + 48x + 72}{(1 + t)^3}. \tag{26}$$

In the computation, the boundary conditions (including those at the ghost points) are given by the exact values, and the time steps are taken such that  $\Delta t = O(\Delta x^{5/3})$ . The  $L_1(-1, 1)$  and  $L_\infty(-1, 1)$  errors between the numerical and smooth solutions are shown in Tables 1 and 2, along with the order of convergence. These results indicate the expected fifth order accuracy of the WENO reconstruction.

It might be also a concern what sort of accuracy is obtained for the test problem in the layered medium. In general, this case includes considerable discontinuities and therefore the same accuracy could not be achieved. The order of convergence with  $L_\infty(-1, 1)$  errors is indicated to be around 1.75 (Table 3) when applying Example 4 and taking the numerical solution with  $h = \Delta x = 0.0125$  to be the “true solution”. The errors are also shown in Fig. 7.

In the above, we set  $\tilde{a}_{j+1/2} = a_{j+1/2}$ . For the biased choices of  $\tilde{a}_{j+1/2} = a_j$  and  $\tilde{a}_{j+1/2} = a_{j+1}$  that are applied in Fig. 6, the test indicates almost the same errors and orders. These errors are indicated with little difference, as are compared in Fig. 8, where Example 4 is also applied with the same parameters except for  $h = 0.05$ .

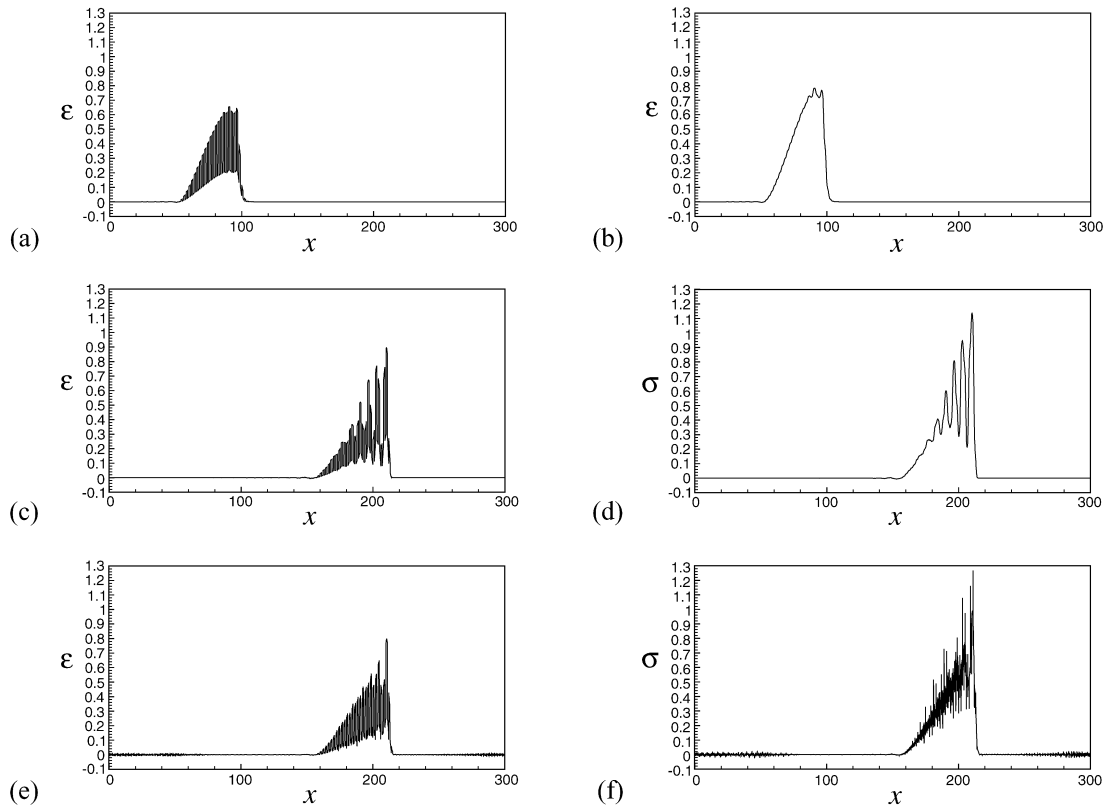


Fig. 4. The strain and stress, (a)–(d) at  $t = 120$  and  $t = 240$  with  $\delta$ -mapping; (e), (f) at  $t = 240$  without  $\delta$ -mapping.

Table 1

$L_1(-1, 1)$  and  $L_\infty(-1, 1)$  errors, and orders of convergence to exact smooth solution (25)

$t = 2$	the strain $\varepsilon$				the velocity $u$			
	$L_1$ error	order	$L_\infty$ error	order	$L_1$ error	order	$L_\infty$ error	order
10	1.97E-04		3.77E-04		1.93E-04		3.25E-04	
20	7.03E-06	4.81	1.34E-05	4.81	8.33E-06	4.54	1.18E-05	4.78
40	2.25E-07	4.97	4.14E-07	5.02	2.97E-07	4.81	3.91E-07	4.92
80	7.04E-09	5.00	1.29E-08	5.01	9.70E-09	4.94	1.29E-08	4.92
160	2.25E-10	4.97	4.45E-10	4.86	3.06E-10	4.98	4.02E-10	5.00
320	7.61E-12	4.88	1.71E-11	4.70	9.45E-12	5.01	1.26E-11	4.99

Table 2

$L_1(-1, 1)$  and  $L_\infty(-1, 1)$  errors, and orders of convergence to exact smooth solution (26)

$t = 1$	the strain $\varepsilon$				the velocity $u$			
	$L_1$ error	order	$L_\infty$ error	order	$L_1$ error	order	$L_\infty$ error	order
10	3.63E-04		6.53E-04		4.62E-04		1.12E-03	
20	9.54E-06	5.25	1.46E-05	5.48	1.36E-05	5.08	3.62E-05	4.95
40	2.74E-07	5.12	4.77E-07	4.94	5.49E-07	4.63	1.16E-06	4.97
80	1.10E-08	4.64	3.94E-08	3.60	2.72E-08	4.33	5.17E-08	4.48
160	5.40E-10	4.35	2.97E-09	3.73	1.42E-09	4.26	3.84E-09	3.75
320	1.89E-11	4.97	1.67E-10	4.15	5.29E-11	4.77	2.16E-10	4.15

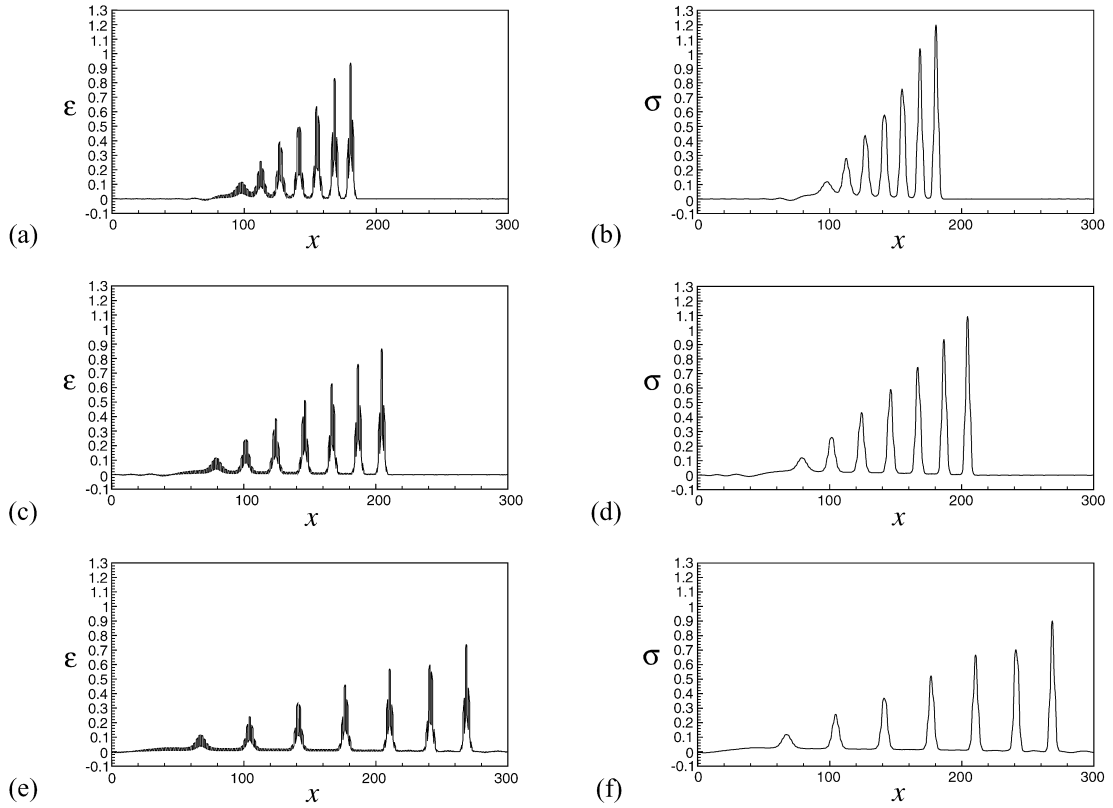


Fig. 5. The strain and stress at (a), (b)  $t = 840$ ; (c), (d)  $t = 1500$ ; and (e), (f)  $t = 2850$ .

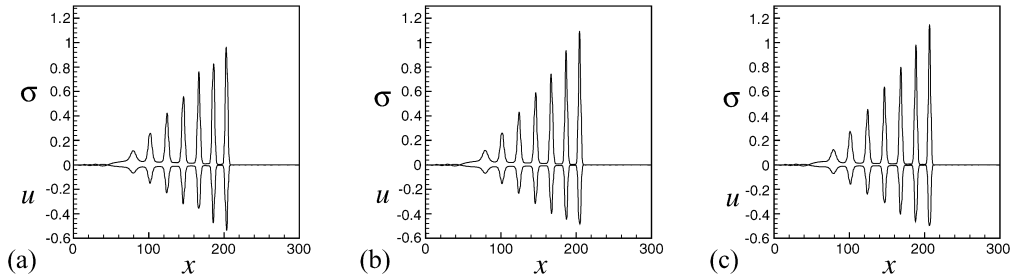


Fig. 6. Comparison among different  $\tilde{a}_{j+1/2}$ , (a)  $\tilde{a}_{j+1/2} = a_j$ ; (b)  $\tilde{a}_{j+1/2} = 0.5(a_j + a_{j+1})$ ; (c)  $\tilde{a}_{j+1/2} = a_{j+1}$ .

Table 3

$L_\infty$  errors and orders of convergence at  $t = 240$ , applying Example 4 and taking numerical solution with  $h = 0.0125$  to be “true” solution

$\Delta x$	$L_\infty$ error of $u$	$L_\infty$ order of $u$	$L_\infty$ error of $\sigma$	$L_\infty$ order of $\sigma$
0.2	9.82E-02		1.93E-01	
0.1	3.29E-02	1.58	6.38E-02	1.6
0.05	9.65E-03	1.77	1.75E-02	1.87
0.025	2.65E-03	1.86	4.51E-03	1.95

#### 4.4. Extension to 2D linear elasticity in heterogeneous media

In this section, the developed scheme is extended to solve the 2D linear elasticity in heterogeneous media. We take the following model equations:

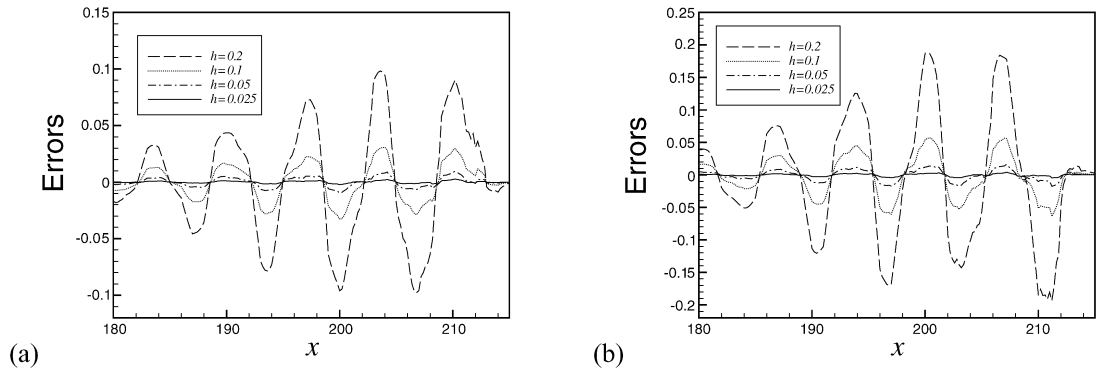


Fig. 7.  $L_\infty$  errors at  $t = 240$  in a grid refinement, applying Example 4 and taking numerical solution with  $h = 0.0125$  to be true solution: (a) the velocity  $u$ ; (b) the stress  $\sigma$ .

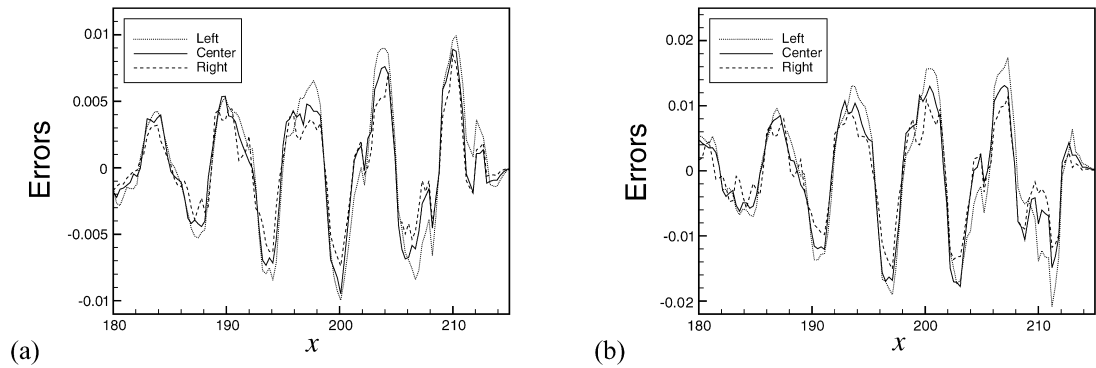


Fig. 8. Comparison of errors among the left-biased ( $\tilde{a}_{j+1/2} = a_j$ ), centered ( $\tilde{a}_{j+1/2} = a_{j+1/2}$ ) and right-biased ( $\tilde{a}_{j+1/2} = a_{j+1}$ ) mappings at  $t = 240$ : (a) the velocity  $u$ ; (b) the stress  $\sigma$ .

$$\begin{aligned} \sigma_t^{11} - (\lambda + 2\mu)u_x - \lambda v_y &= 0, \\ \sigma_t^{22} - \lambda u_x - (\lambda + 2\mu)v_y &= 0, \\ \sigma_t^{12} - \mu(v_x + u_y) &= 0, \\ \rho u_t - \sigma_x^{11} - \sigma_y^{12} &= 0, \\ \rho v_t - \sigma_x^{12} - \sigma_y^{22} &= 0, \end{aligned}$$

which describe both P- and S-waves in the  $x-t$  plane and are known as the Plane-Strain equations. Here,  $\sigma^{11}, \sigma^{22}$  are normal stress components in  $x, y$  directions, and  $\sigma_{12}$  is the shear stress;  $\lambda$  and  $\mu$  are the Lamé parameters of the material, which are also the functions of spatial variables in heterogeneous media. See [10] for more descriptions about this model.

Through the introduction of the new variables:

$$Q_1 = \frac{\sigma^{11} + \sigma^{22}}{2(\lambda + \mu)}, \quad Q_2 = \frac{\sigma^{11} - \sigma^{22}}{2\mu}, \quad Q_3 = \frac{\sigma^{12}}{\mu}, \quad Q_4 = \rho u, \quad Q_5 = \rho v,$$

the system can be rewritten in the following conservation form:

$$U_t + F(U, a)_x + G(U, a)_y = 0, \tag{27}$$

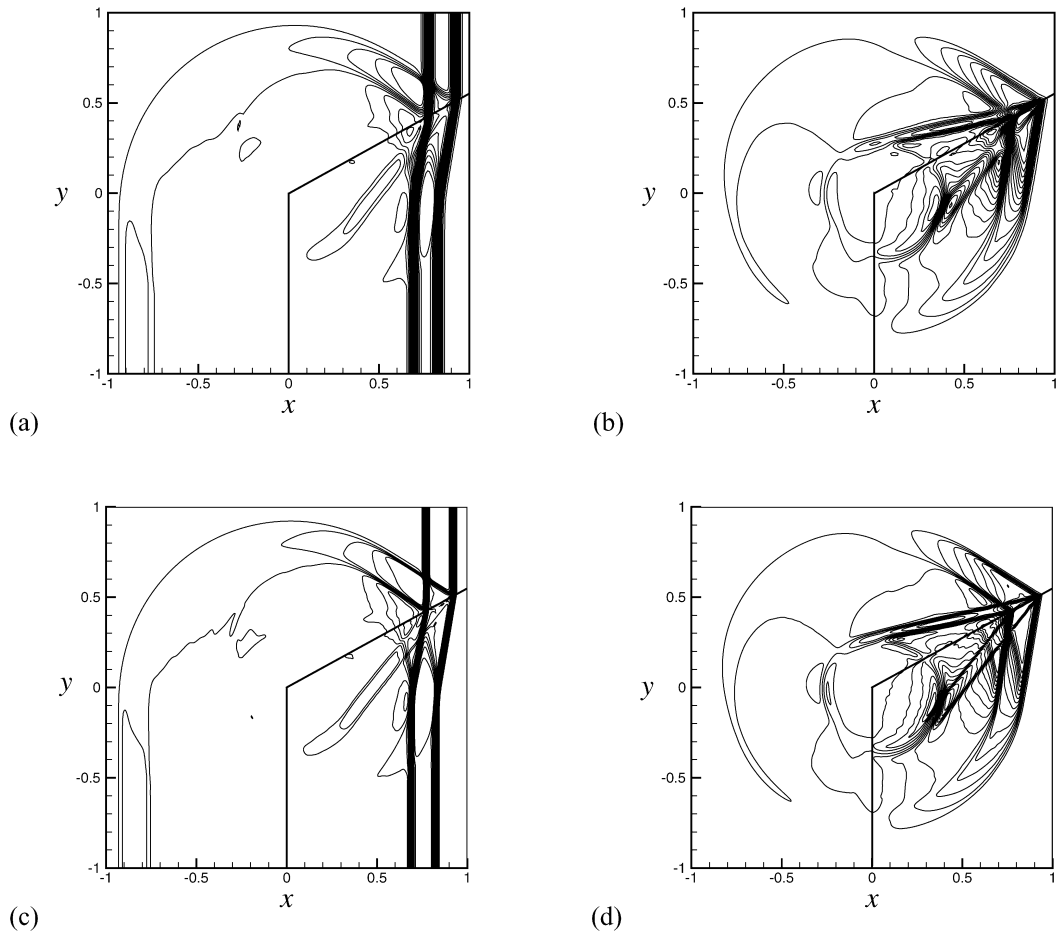


Fig. 9. Numerical results of the stresses  $\sigma^{11}$  and  $\sigma^{12}$  with two different grid points  $200 \times 200$  (a,b) and  $400 \times 400$  (c,d). (a,c) 30 contours of  $\sigma^{11}$  from  $-0.8$  to  $4.8$ ; (b,d) 30 contours of  $\sigma^{12}$  from  $-0.39$  to  $0.16$ .

with

$$U = \begin{pmatrix} Q_1 \\ Q_2 \\ Q_3 \\ Q_4 \\ Q_5 \end{pmatrix}, \quad F(U, a) = \begin{pmatrix} -Q_4/\rho \\ -Q_4/\rho \\ -Q_5/\rho \\ (\lambda + \mu)Q_1 + \mu Q_2 \\ \mu Q_3 \end{pmatrix}, \quad G(U, a) = \begin{pmatrix} -Q_5/\rho \\ Q_5/\rho \\ -Q_4/\rho \\ \mu Q_3 \\ (\lambda + \mu)Q_1 - \mu Q_2 \end{pmatrix}. \quad (28)$$

Note that these functions of spatial variables are represented by the vector  $a = (\rho(x, y), \lambda(x, y), \mu(x, y))$ .

To solve this 2D system, the numerical scheme of (2) can be easily extended in a way of “dimension by dimension”; see (for example) [17] for more details. Therefore, it is similar to achieve a local “standardization” in a numerical flux through the  $\delta$ -mapping algorithm and then apply the WENO reconstruction to obtain the numerical fluxes. In this case, we acquire  $\delta U_{i+l, j+m}$ , for  $l, m = -2, -1, \dots, 3$ , from the following equations:

$$\begin{aligned} (Q_4)_{i+l, j+m} / \rho_{i+l, j+m} &= \tilde{\delta}(Q_4)_{i+l, j+m} / \tilde{\rho}_{ij}, \\ (Q_5)_{i+l, j+m} \rho_{i+l, j+m} &= \tilde{\delta}(Q_5)_{i+l, j+m} \tilde{\rho}_{ij}, \\ \mu_{i+l, j+m} (Q_3)_{i+l, j+m} &= \tilde{\mu}_{ij} \tilde{\delta}(Q_3)_{i+l, j+m}, \\ (\lambda_{i+l, j+m} + \mu_{i+l, j+m}) (Q_1)_{i+l, j+m} &= (\tilde{\lambda}_{ij} + \tilde{\mu}_{ij}) \tilde{\delta}(Q_1)_{i+l, j+m}, \\ \mu_{i+l, j+m} (Q_2)_{i+l, j+m} &= \tilde{\mu}_{ij} \tilde{\delta}(Q_2)_{i+l, j+m}. \end{aligned}$$

We consider such a heterogeneous medium that consists of two different materials, with the parameters

$$\rho_A = 1, \quad \lambda_A = 4, \quad \mu_A = 0.5; \quad \rho_B = 1, \quad \lambda_B = 2, \quad \mu_B = 1,$$

in the domain  $[-1, 1] \times [-1, 1]$ . We suppose that the region of  $x > 0$  and  $y < 0.55x$  is filled with material B, and that other regions are filled with material A. The initial data are taken as

$$\sigma^{11} = 5, \quad \sigma^{22} = 4, \quad \sigma^{12} = 0, \quad u = -\sqrt{5}, \quad v = 0,$$

for  $-0.35 < x < -0.2$ , and zero elsewhere.

The initial values suggest a right-going P-wave (along  $x$  direction) in that  $U$  is a right eigenvector of the Jacobian  $F_U(U, a)$ . After hitting the interface, the transmitted P-wave moves more slowly in material B, and a partial reflection appears. Numerical results of  $\sigma^{11}$  and  $\sigma^{12}$  at time  $t = 0.5$  are shown in Fig. 9, with the time step  $\Delta t = 0.4\Delta x/\sqrt{5}$  and two different grid points  $200 \times 200$  and  $400 \times 400$ . From the figure, the transmitted and reflected P-waves are clearly observed, and the S-waves go clearly along the ramp portion of the interface. These suggest an excellent convergence when compared with the known numerical results (e.g., in [10]).

In this example, we note that the computational time is controlled such that the propagation does not reach  $x = \pm 1$ , thus the left and right boundary (namely all needed ghost point) values remain zero. Since there is no propagation in  $y$  direction, we only need to set

$$U_y(x, \pm 1, t) = 0$$

to describe the change of solution that is due to the propagation along the boundaries  $y = \pm 1$ . By the zero-order extrapolation, this suggests that all ghost point values of  $U(x, -1, t)$  or  $U(x, 1, t)$  equal to the proximal one in the computational domain. See also [10] for similar treatment.

For a longer computation, we note that such special treatment as ABCs or PMLs is needed to sustain the wave propagation in unbounded domains in  $x$  direction. See [5,19] for this account.

## 5. Conclusions

By extension, we develop the  $\delta$ -mapping algorithm for solving the elastic waves in heterogeneous media. This algorithm is coupled with the WENO method to constitute a complete scheme. In solving the model system which possesses spatially varying flux functions, this scheme is advantageous because its numerical flux is consistent with steady solutions in comparison with a classical numerical flux which is only consistent with trivial solutions. Therefore, as compared with the WENO scheme itself, this scheme generates highly resolved numerical results.

For further extension of the  $\delta$ -mapping algorithm, we emphasize that

- (a) it can be coupled with other well developed numerical methods (e.g., the RKDG and TVD schemes) in solving similar problems;
- (b) it can be directly and widely applied in many physical problems wherever the mapping is explicit and unique; and
- (c) for problems in which case the mapping is implicit, alternatives of the mapping should be developed for efficient computation.

## Acknowledgements

This work was jointly supported by Natural Science Foundation of China (10472064, 10371118) and the National Key Laboratory of Computational Physics in Beijing. The authors thank Professor Randall J. LeVeque, Department of Applied Mathematics, University of Washington, for his instructive comments. The authors also thank the anonymous referee for his many suggestions in the earlier draft of this paper.

## References

- [1] D.B. Bale, R.J. LeVeque, S. Mitran, A. Rossmannith, A wave propagation method for conservation laws and balance laws with spatially varying flux functions, *SIAM J. Sci. Comput.* 24 (2002) 955–978.
- [2] D. Balsara, C.-W. Shu, Monotonicity preserving weighted essentially non-oscillatory schemes with increasingly high order accuracy, *J. Comput. Phys.* 160 (2000) 405–452.

- [3] B. Cockburn, C.-W. Shu, Runge–Kutta discontinuous Galerkin methods for convective-dominated problems, *J. Sci. Comput.* 16 (3) (2001) 173–261.
- [4] T.R. Fogarty, R.J. LeVeque, High-resolution finite volume methods for acoustics in periodic or random media, *J. Acoust. Soc. Amer.* 106 (1999) 17–28.
- [5] D. Givoli, *Numerical Methods for Problems in Infinite Domains*, Elsevier, Amsterdam, 1992.
- [6] S. Gottlieb, C.-W. Shu, E. Tadmor, Strong stability preserving high order time discretization method, *SIAM Rev.* 43 (2001) 89–112.
- [7] A. Harten, B. Engquist, S. Osher, S. Chakaravathy, Uniformly high order accurate essentially non-oscillatory schemes III, *J. Comput. Phys.* 71 (1987) 231–303.
- [8] C. Hu, C.-W. Shu, Weighted essentially non-oscillatory schemes on triangular meshes, *J. Comput. Phys.* 150 (1999) 97–127.
- [9] G.S. Jiang, C.-W. Shu, Efficient implementation of weighted ENO schemes, *J. Comput. Phys.* 126 (1996) 202–228.
- [10] R.J. LeVeque, *Finite Volume Methods for Hyperbolic Problems*, Cambridge University Press, Cambridge, 2002.
- [11] R.J. LeVeque, Finite-volume methods for non-linear elasticity in heterogeneous media, *Internat. J. Numer. Methods Fluids* 40 (2002) 93–104.
- [12] R.J. LeVeque, D.H. Yong, Solitary waves in layered nonlinear media, *SIAM J. Appl. Math.* 63 (2003) 1539–1560.
- [13] D. Levy, G. Puppo, G. Russo, A third order central WENO scheme for 2D conservation laws, *Appl. Numer. Math.* 33 (2000) 415–421.
- [14] X.-D. Liu, S. Osher, T. Chan, Weighted essentially non-oscillatory schemes, *J. Comput. Phys.* 115 (1994) 200–212.
- [15] B. Lombard, J. Piraux, Numerical treatment of two-dimensional interfaces for acoustic and elastic waves, *J. Comput. Phys.* 195 (2004) 90–116.
- [16] J.X. Qiu, C.-W. Shu, On the construction, comparison and local characteristic decomposition for high order central WENO schemes, *J. Comput. Phys.* 183 (2002) 187–209.
- [17] C.-W. Shu, Essentially non-oscillatory and weighted essentially non-oscillatory schemes for hyperbolic conservation laws, ICASE Report No. 1997-65.
- [18] C.-W. Shu, Total-Variation-Diminishing time discretizations, *SIAM J. Sci. Stat. Comput.* 9 (1988) 1073–1084.
- [19] S.V. Tsynkov, Numerical solution of problems on unbounded domains. A review, *Appl. Numer. Math.* 27 (1998) 465–532.
- [20] P. Zhang, R.X. Liu, Hyperbolic conservation laws with space-dependent flux: I. Characteristics theory and Riemann problem, *J. Comput. Appl. Math.* 156 (2003) 1–21.
- [21] P. Zhang, R.X. Liu, Generalization of Runge–Kutta discontinuous Galerkin method to LWR traffic flow model with inhomogeneous road conditions, *Numer. Methods Partial Differential Equations* 21 (1) (2005) 80–88.
- [22] P. Zhang, R.X. Liu, Hyperbolic conservation laws with space-dependent flux: II. General study of numerical fluxes, *J. Comput. Appl. Math.* 176 (2005) 105–129.